SCIENTIFIC REPORTS

OPEN

Absence of Structural Impact of Noble Nanoparticles on P3HT:PCBM Blends for Plasmon-Enhanced Bulk-Heterojunction Organic Solar Cells Probed by Synchrotron GI-XRD

Samuele Lilliu[1], Mejd Alsari[1], Oier Bikondoa[2], J. Emyr Macdonald[3] & Marcus S. Dahlem[1]

The incorporation of noble metal nanoparticles, displaying localized surface plasmon resonance, in the active area of donor-acceptor bulk-heterojunction organic photovoltaic devices is an industrially compatible light trapping strategy, able to guarantee better absorption of the incident photons and give an efficiency improvement between 12% and 38%. In the present work, we investigate the effect of Au and Ag nanoparticles blended with P3HT: PCBM on the P3HT crystallization dynamics by synchrotron grazing incidence X-ray diffraction. We conclude that the presence of (1) 80 nm Au, (2) mix of 5 nm, 50 nm, 80 nm Au, (3) 40 nm Ag, and (4) 10 nm, 40 nm, 60 nm Ag colloidal nanoparticles, at different concentrations below 0.3 wt% for Au and below 0.1% for Ag in P3HT: PCBM blends, does not affect the behaviour of the blends themselves.

In the photovoltaics community it is commonly believed that in order to attract useful market shares, organic photovoltaic (OPV) solar cell efficiency must be higher than 10% for roll-to-roll-processed modules. In 2014, the best performing polymer lab-based triple junction devices achieved a power conversion efficiency (PCE) of ~11.5%[1]. The photoactive area of the OPV devices discussed here is based on the bulk-heterojunction (BHJ) concept[2–4]. A BHJ is a thin film consisting of a blend between: (i) a p-doped electron-donor/hole-transporter phase (e.g. a polymer), and (ii) n-type, hole-donor/electron-transporter phase (e.g. a fullerene). Single junction OPVs typically consist of the following stacked layers: glass substrate, transparent conductive oxide, hole-donor interlayer (e.g. PEDOT: PSS), BHJ active layer (e.g. P3HT: PCBM), and top electrode (e.g. Ca/Al). In contrast to inorganic photovoltaic devices, OPVs are described as excitonic solar cells, to indicate that sufficiently energetic photons do not promptly produce free charges, but rather generate excitons[5]. Efficient charge harvesting from incoming photons imposes several morphological and optoelectrical constraints on the BHJ. The ideal BHJ nanostructure is a compromise between complete separation of the donor-acceptor phases and close interpenetration[5]. High recombination rate and low charge-carrier mobility limit the BHJ thickness to below 100-200 nm. This restricts the absorption yield and the resulting PCE[6]. Effective light trapping strategies offer a good approach to ensure better absorption of the incident photons, and a route for attaining efficiencies beyond the 10% barrier for single junction OPV, which would push the commercialization of organic solar cells[6].

[1]Masdar Institute of Science and Technology, PO Box 54224, Abu Dhabi, United Arab Emirates. [2]XMaS, The UK-CRG Beamline, ESRF-The European Synchrotron, CS40220, 38043 Grenoble Cedex 9, France. [3]School of Physics and Astronomy, Cardiff University, Queens Buildings, The Parade, Cardiff CF24 3AA, United Kingdom. Correspondence and requests for materials should be addressed to S.L. (email: samuele_lilliu@hotmail.it)

Plasmonic nanostructures can be incorporated into the active area of organic solar cells to enhance the optical absorption and the current density, without increasing the thickness of their active areas[6]. Noble metal nanoparticles (NPs), such as Au and Ag, exhibit Localized Surface Plasmon Resonance (LSPR) that couple strongly to the incident light[7]. This effect can increase the light absorption capability of the OPV device within a broad range of wavelengths[7–10]. This strategy is highly compatible with industrial roll-to-roll OPV fabrication processes, since the NPs are easily blended within the BHJ solution. To date, the most relevant research in this field includes the following works[8,9,11–15]. The authors demonstrate that plasmon enhanced bulk-heterojunction OPVs show a PCE increase of 12–38%, when compared to control devices without NPs. Still missing in the literature is a comprehensive structural investigation of NPs enhanced OPVs, and a discussion on the correlation between structural properties of the films and device properties. A Grazing Incidence Wide Angle X-Ray Scattering (GI-WAXS) study recently showed that, by introducing Cu_2S NPs in the BHJ, the self-organized nano-structural evolution of the donor-acceptor phases can be finely tuned[16]. The main question is whether a similar effect can be observed with noble metal NPs blended with P3HT: PCBM. The investigation of donor-acceptor Grazing Incidence X-Ray Diffraction (GI-XRD) patterns before and after the annealing is a powerful tool for understanding the evolution dynamics of the nano-morphology of the two materials during thermal or solvent annealing[17–22]. Information extracted from GI-XRD patterns of NPs enhanced BHJ could be correlated to other studies to improve understanding of the morphological factors affecting the overall OPV performance[18].

To the best of our knowledge, there are not any reported comprehensive synchrotron GI-XRD investigations on the effects of Au and Ag NPs on the structural properties of the donor-acceptor phases in OPVs bulk-heterojunctions. In this work we investigate the effect of the presence of Au and Ag NPs in the P3HT: PCBM bulk-heterojunction on the semi-crystalline P3HT phase.

Experimental Details

Colloidal Au nanoparticles suspended in a citrate buffer solution were purchased from Sigma-Aldrich (5 nm, 741949-25 ML, 50 nm, 742007–25 ML, 80 nm, 742023–25 ML). Colloidal Ag nanoparticles dispersed in aqueous buffer containing sodium citrate as the stabilizer were purchased from Sigma-Aldrich (10 nm, 730785–25 ML, 40 nm, 730807–25 ML, 60 nm, 730815–25 ML). Regioregular poly(3-hexylthiophene-2,5-diyl) (P3HT) was purchased from Ossila Ltd (M107, RR 93.6%, Mw 31,300, Mn 15,600). A mixture of [6,6]-Phenyl-C71-butyric acid methyl ester (PC70BM) and [6,6]-Phenyl-C61-butyric acid methyl ester (PC60BM) (95/5%) was purchased from Ossila Ltd (M113). Silicon oxide (Si/SiO$_2$) substrates were purchased from Ossila Ltd, and cleaved into substrates smaller than 1 cm^2. The substrates were cleaned by sonication in water with Hellmanex (Z805939, FLUKA), deionized water, acetone, isopropanol, and water (15 min each). A P3HT: PCBM solution was prepared by dispersing 25 mg/mL of P3HT and PCBM (1:0.6) in chlorobenzene. The solution was stirred at 80 °C for 10 min and overnight at 50 °C. Twelve 4 mL vials containing different amounts of nanoparticles were left on a hotplate at 100 °C for several hours until the solvent was completely evaporated[23]. 33 mL of P3HT: PCBM blend was then added to each vial. The final solution was stirred overnight at 50 °C. The list of solutions and P3HT: PCBM: NPs wt% is reported in Table 1. 'Au mix' refers to a mix between 5 nm (33%), 50 nm (33%) and 80 nm (33%) Au nanoparticles. 'Ag mix' refers to a mix between 10 nm (33%), 40 nm (33%) and 60 nm (33%) Ag nanoparticles. The solutions were prepared in a nitrogen filled glovebox (H$_2$O < 0.1 ppm, O$_2$ < 0.1 ppm). Each solution was spin-coated on the clean silicon oxide substrates at 2000 rpm for 30 min under nitrogen atmosphere. Half of the samples were ex-situ annealed before the XRD measurements for 15 min at 150 °C.

The average sample thickness was 100 nm. Details of our GI-XRD setup and geometry have already been reported[17,19,22,24,25]. GI-XRD measurements were performed at the XMaS beamline (BM28, ESRF, Grenoble, France). Diffraction images were collected with a 2D detector (MAR SX-165). The X-ray energy was 10 keV. The critical angle of the films was $\alpha_c \approx 0.12°$, and measurements were taken at different incident angles α_i below and above the critical angle. The Matlab software developed by Dr. Lilliu for the GI-XRD analysis[17] was updated with a new routine for total image remapping into the scattering vector (q) space. The $q_{xy} = 0$, $q_z = 1$ [Å^{-1}] coordinate on the diffraction images corresponds to the azimuthal angle $\chi = 0°$ (out-of-plane direction, or OOP), while the $q_{xy} = 1$, $q_z = 0$ [Å^{-1}] direction, corresponds to $\chi = 90°$ (in-plane direction, or IP). Therefore, due to the experimental geometry, the cake slice corresponding to $\chi = 0°$ is not accessible in the reported diffraction images (black background). Line profiles are extracted from cake slices at different azimuthal angles with an integration aperture of $\Delta\chi = 10°$. Peak fitting is performed as previously reported[17].

Results and Discussion

Following the study shown by Liao et al. on the effect of Cu_2S NPs on the nano-structural evolution of the donor-acceptor phases[16], we investigate the effect of commercial Au and Ag NPs in the P3HT: PCBM bulk-heterojunction. The colloidal NPs employed here, have an absorption spectrum[26] that overlaps with the visible spectrum and can be employed in the fabrication of OPVs based on plasmon enhanced BHJ. NPs have a bell-like absorption spectrum with a peak in the visible that varies with the size of the NPs. Mixing NPs with different sizes allows achieving a broad absorption spectrum and the possibility to exploit the plasmonic effect on a broader range of wavelengths.

Figure 1 shows diffraction patterns collected at $\alpha_i = 0.12°$ for P3HT: PCBM: Au NPs films before and after ex-situ annealing. Images (a-f) are from blends mixed with 80 nm Au NPs (solutions 1–3 in
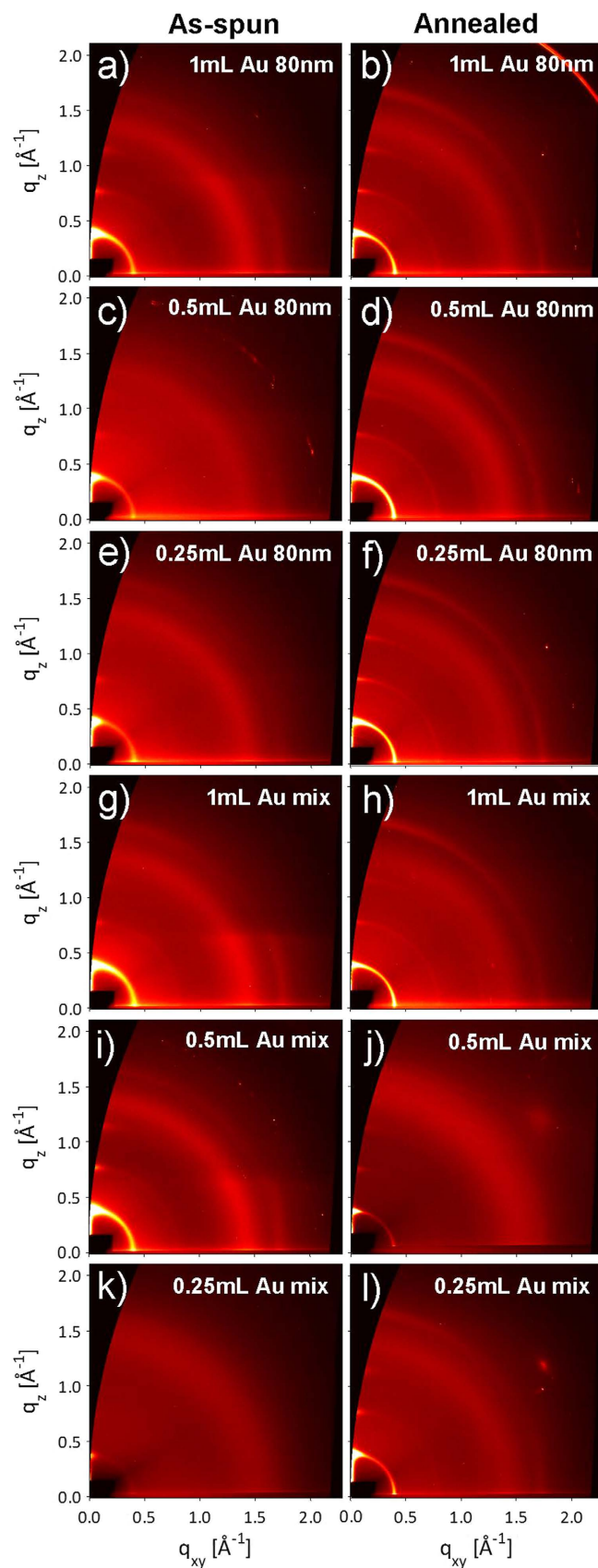
Figure 1. Diffraction images collected at the critical angle for as-spun and annealed P3HT: PCBM: Au NPs blends: (a-b) Au 80 nm 1 mL, (c-d) Au 80 nm 0.5 mL, (e-f) Au 80 nm 0.25 mL, (g-h) Au mix 1mL, (i-j) Au mix 0.5 mL, and (k-l) Au mix 0.25 mL.

Solution number	NPs	Amount	P3HT%	PCBM%	NPs%
1	Au 80nm	1mL	62.37	37.42	0.20
2	Au 80nm	0.5mL	62.44	37.46	0.10
3	Au 80nm	0.25mL	62.47	37.48	0.05
4	Au mix	1mL	62.33	37.40	0.28
5	Au mix	0.5mL	62.41	37.45	0.14
6	Au mix	0.25mL	62.48	37.49	0.03
7	Ag 40nm	1mL	62.45	37.47	0.08
8	Ag 40nm	0.5mL	62.48	37.49	0.04
9	Ag 40nm	0.25mL	62.49	37.49	0.02
10	Ag mix	1mL	62.45	37.47	0.08
11	Ag mix	0.5mL	62.48	37.49	0.04
12	Ag mix	0.25mL	62.49	37.49	0.02

Table 1. P3HT: PCBM: Au/Ag NPs solutions, amount of NPs from the as-received solution, and P3HT: PCBM: NPs wt%.
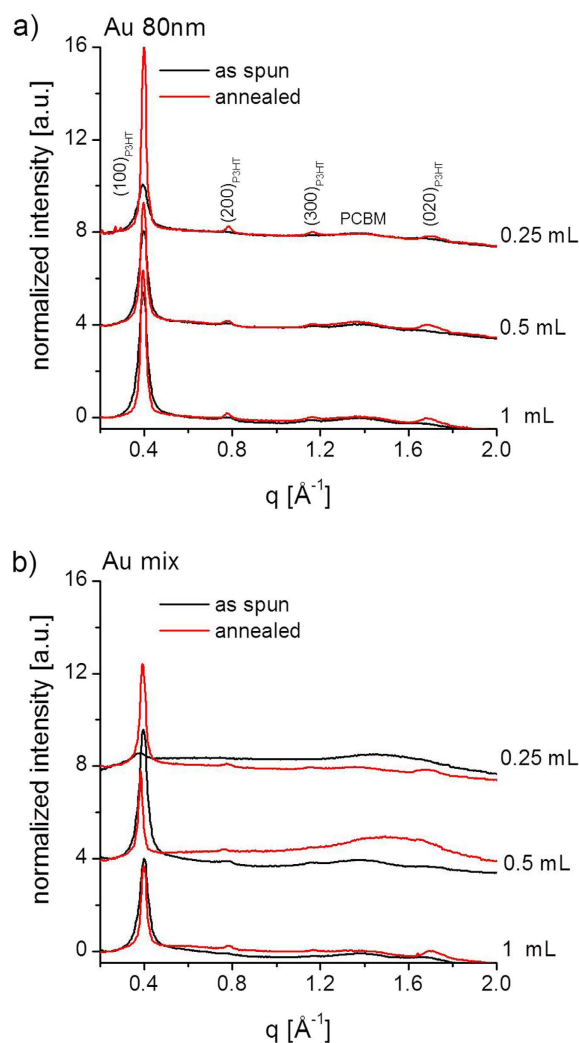
Figure 2. Line profiles collected at critical angle, extracted with cake slices centred at $\chi = 15°$ ($\Delta\chi = 10°$ integration aperture), for films deposited from P3HT: PCBM: Au NPs solutions (1–6), measured ex-situ before and after annealing. All line profiles are normalized with respect to the line profile region between the end of the beamstop and the beginning of the first peak, the (100)-P3HT peak. P3HT and PCBM peaks are indicated in (a).
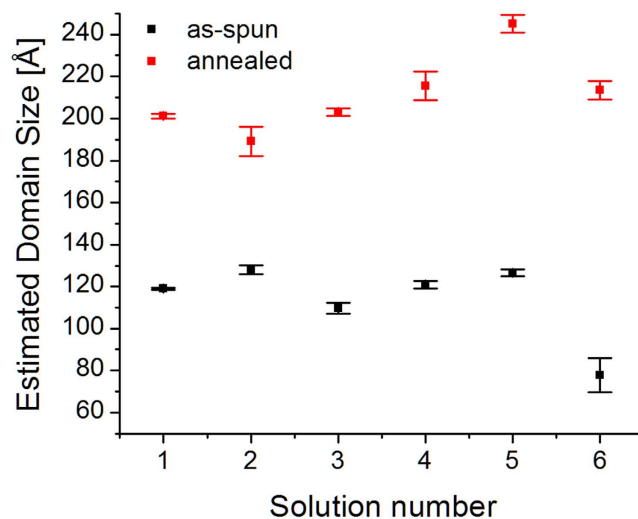
Figure 3. (100)-P3HT domain sizes estimated with the Scherrer equation for P3HT: PCBM: Au NPs. Statistics are performed on several images collected at different angles above $\alpha i = 0.16°$, in particular: (i) as-spun samples, 10 for solution 1 (80 nm, 1 mL), 3 for solution 2 (80 nm, 0.5 mL), 9 for solution 3 (80 nm, 0.25 mL), 10 for solution 4 (mix, 1 mL), 4 for so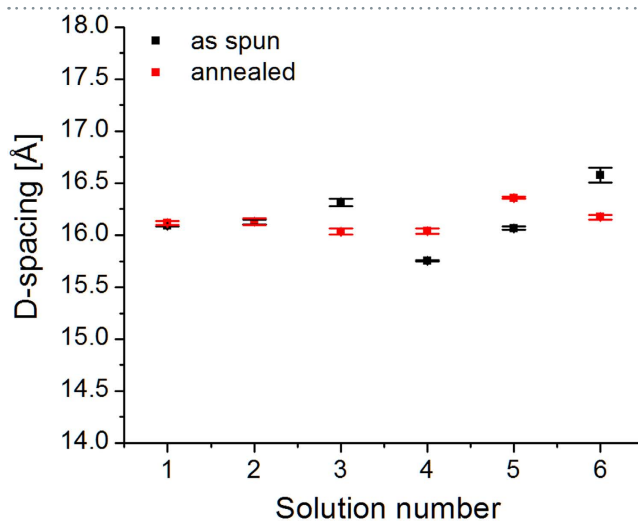lution 5 (mix, 0.5 mL), and 14 for solution 6 (mix, 0.25 mL); (ii) annealed samples, 5 for solution 1 (80 nm, 1 mL), 7 for solution 2 (80 nm, 0.5 mL), 5 for solution 3 (80nm, 0.25 mL), 6 for solution 4 (mix, 1 mL), 15 for solution 5 (mix, 0.5 mL), and 13 for solution 6 (mix, 0.25 mL).

Figure 4. (100)-P3HT lattice constant along the a-direction of the alkyl-stacking chains for P3HT: PCBM: Au NPs. See Fig. 3 for information on the statistics.

Table 1), while images (g-l) are from blends with a mix of 5 nm, 50 nm and 80 nm (solutions 4–6 in Table 1). Fig. 2 shows lineprofiles extracted along the OOP direction ($\chi = 15°$), for the blends with (a) 80 nm Au NPs, and (b) Au mix.

The diffraction patterns resemble those reported in our previous work, and diffraction peaks have been indexed accordingly[17,19,22]. P3HT crystallizes with a monoclinic unit cell[17,27], and self-organizes into lamellar structures[28–31]. In the lamella, the backbones are oriented along the c-direction. Continuous lamellae are stacked (i) orthogonal to the parallel conjugated backbones in the b-direction and (ii) along the alkyl-stacking a-direction[17]. The alkyl-stacking direction can be perpendicular (edge-on lamellae) to the sample substrate or parallel to the sample substrate (face-on lamellae)[17]. PCBM crystallizes from chlorobenzene with a triclinic unit cell, and does not preferentially orientate with respect to the sample substrate, under usual processing conditions[17,32,33].

In order to verify whether the presence of NPs in the blend induces structural changes in the semi-crystalline phase of P3HT, line profiles extracted at $\chi = 15°$ for angles above the critical angle are fitted as previously described[17,19,22,24]. At these angles, the retrieved information comes both from
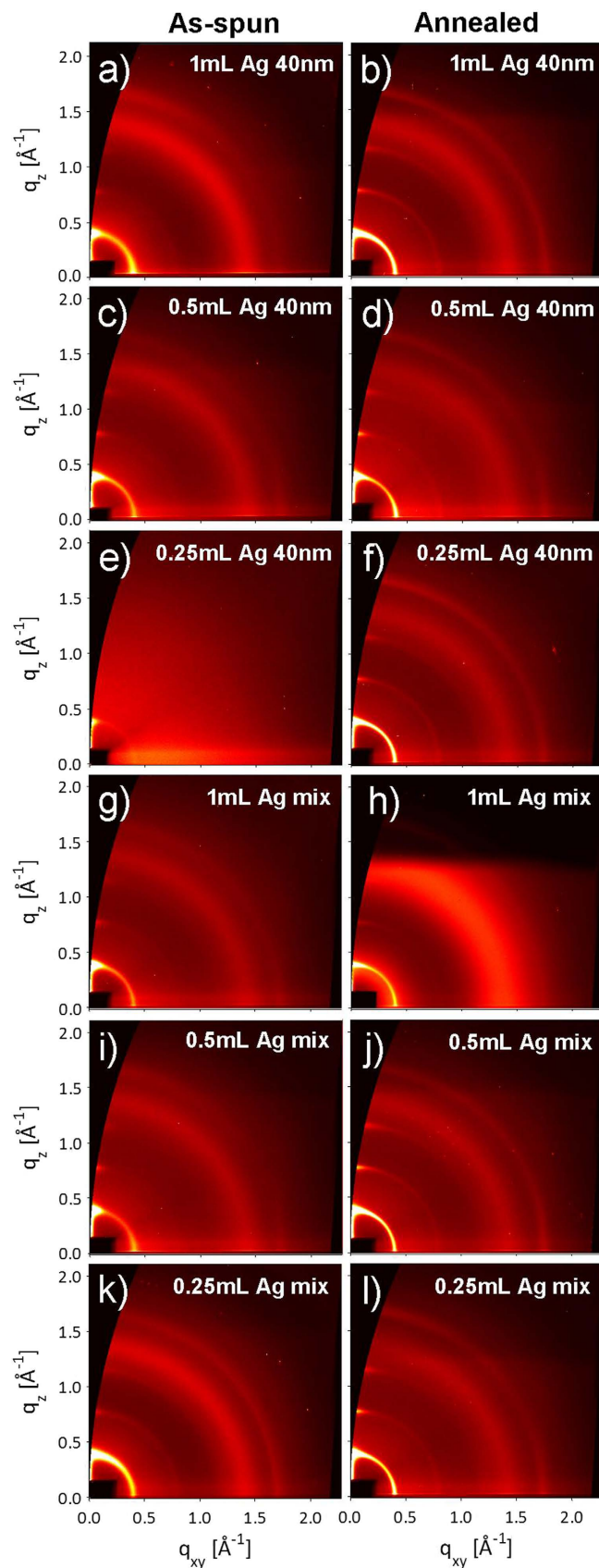
Figure 5. Diffraction images collected at the critical angle for as-spun and annealed P3HT: PCBM: Ag NPs blends: (a-b) Ag 40 nm 1 mL, (c-d) Ag 40 nm 0.5 mL, (e-f) Ag 40 nm 0.25 mL, (g-h) Ag mix 1mL, (i-j) Ag mix 0.5 mL, and (k-l) Ag mix 0.25 mL. Images are extracted at the critical angle in order to display the maximum intensity.
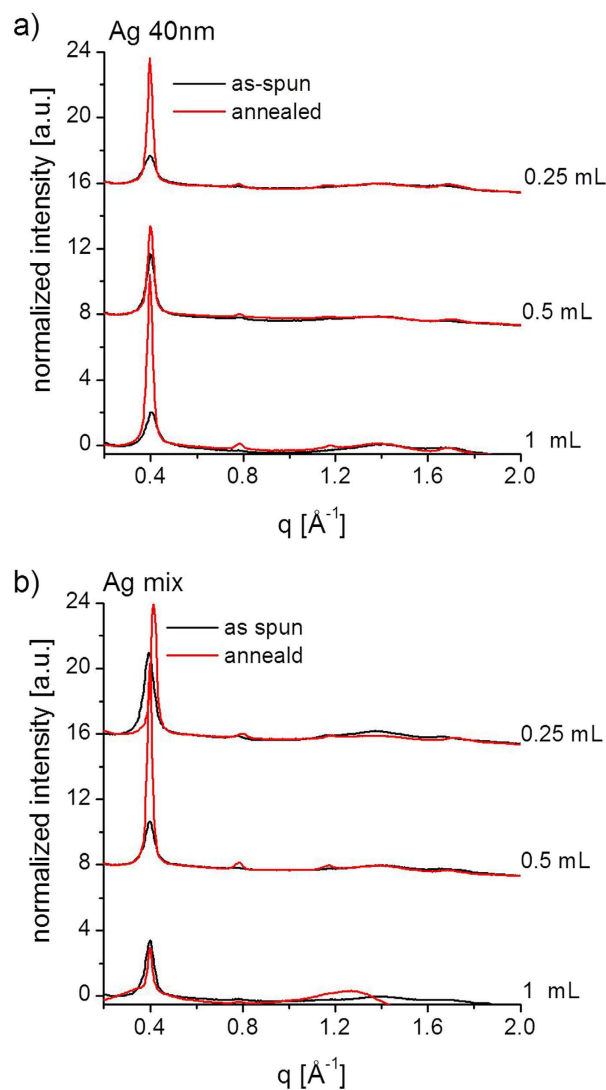
Figure 6. Line profiles collected at critical angle, extracted with cake slices centred at $\chi = 15°$ ($\Delta\chi = 10°$ integration aperture), for films deposited from P3HT: PCBM: Ag NPs solutions (7–12), measured ex-situ before and after annealing. All line profiles are normalized with respect to the line profile region between the end of the beamstop and the beginning of the first peak, (100)-P3HT peak. The line profile drop near $q = 1.5$ Å-1 for the annealed 1mL in (**b**) is due to background issues.

the bulk and the surface. The P3HT domain size along the *a*-direction of the alkyl side chains is estimated from the full width at half maximum (FWHM) of the (100)-P3HT peaks. The estimated domain sizes are calculated using the Scherrer equation[34], i.e. $L_{100} \approx 0.9 \times 2\pi$ / FWHM, which usually overestimates the real domain size and does not take into account disorder contributions in the peak broadening[17]. The purpose of this initial analysis is to verify whether there are significant differences in L_{100} among different samples. Fig. 3 shows the estimated domain sizes L_{100} for the 6 spin-coated solutions. It is clear that different concentrations of NPs do not affect the domain size, and that the difference in L_{100} between samples is simply due to stochastic effects. A common aspect to all the samples is the well-known increase in the P3HT domain size due to the crystallization induced by the anneal[17].

Given the result, further investigation, such as the Williamson-Hall or the Warren-Averbach[34] analysis for the separation of the correlation length contribution from the disorder contribution in the peak broadening, would not add any significant information.

Figure 4 shows the estimated P3HT lattice constant along the *a*-direction of the alkyl-stacking chains. Refraction effects have not been taken into account. The (100)-P3HT peak plots vs α_i (not shown) all show the characteristic profile, with a peak located at the critical angle $\alpha_c = 0.12°$, with the exception of Au mix 0.5 mL, which was misaligned. Again, we do not observe any trend as a function of different
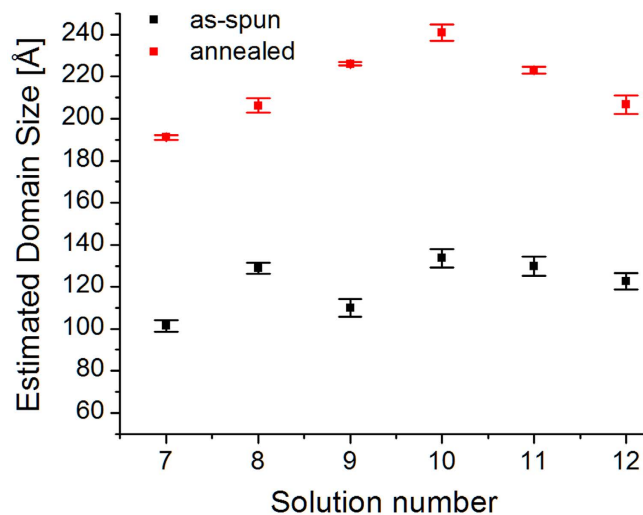
Figure 7. (100)-P3HT domain sizes estimated with the Scherrer equation for P3HT: PCBM: Ag NPs. Statistics are performed on several images collected at different angles above αi = 0.16°, in particular: (i) as-spun samples, 11 for solution 7 (40 nm, 1 mL), 13 for solution 8 (40 nm, 0.5 mL), 8 for solution 9 (40 nm, 0.25 mL), 6 for solution 10 (mix, 1 mL), 12 for solution 11 (mix, 0.5 mL), and 8 for solution 12 (mix, 0.25 mL); (ii) annealed samples, 10 for solution 7 (40 nm, 1 mL), 12 for solution 8 (40 nm, 0.5 mL), 10 for solution 9 (40 nm, 0.25 mL), 11 for solution 10 (mix, 1 mL), 11 for solution 11 (mix, 0.5 mL), and 11 for solution 12 (mix, 0.25 mL).
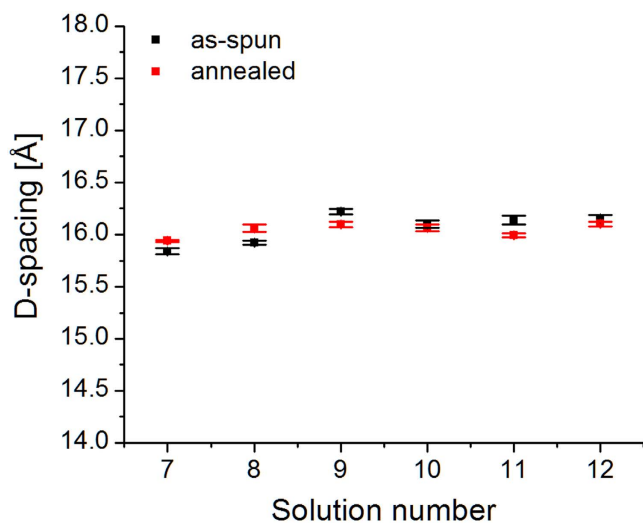

Figure 8. (100)-P3HT lattice constant along the a-direction of the alkyl-stacking chains for P3HT: PCBM: Ag NPs. See Fig. 7 for information on the statistics.

concentrations of Au NPs. A common characteristic observed in the literature is the expansion of the a lattice constant after the anneal[17]. Interestingly, this condition is not verified for both samples containing 0.25 mL of NPs.

The same type of analysis is performed for the samples containing Ag. Fig. 5 shows diffraction patterns collected at the critical angle for P3HT: PCBM: Ag NPs films before and after ex-situ annealing. Images (a-f) are from blends mixed with 40 nm Ag NPs (solutions 7–9 in Table 1), while images (g-l) are from blends with a mix of 10 nm, 40 nm and 60 nm (solutions 10–12 in Table 1). Fig. 6 shows lineprofiles extracted along the OOP direction (χ = 15°), for the blends with (a) 40 nm Ag NPs, and (b) Ag mix.

Figure 7 shows the estimated (100)-P3HT domain size for the samples with Ag NPs. The trend observed for the annealed samples from solutions with 40 nm Ag NPs (7–9) is opposite to the trend observed for the samples prepared with the mix solutions (10–12). Apart from the as-spun sample from solution 8, as-spun samples follow the same trend of the annealed samples. The estimated domain sizes L_{100} are within the same range of values shown for the samples containing Au NPs. Similarly to the

samples containing Au NPs, we believe the difference in (100)-P3HT domain sizes between samples is simply due to stochastic effects. Fig. 8 shows the estimated lattice constant along the *a*-direction. Also in this case, we do not observe any trend as a function of the concentration of NPs. A qualitative comparison between the estimated lattice constants in Figs. 4 and 8 indicates that the graphs are not correlated.

Conclusion

The experiments presented in this work were carried out to investigate the potential effect of noble nanoparticles on the structural properties of the semi-crystalline P3HT phase in P3HT: PCBM blends, used in plasmon enhanced organic bulk-heterojunction solar cells. We conclude that there is no observable correlation between the concentration of nanoparticles dispersed in the P3HT: PCBM blend and the estimated P3HT domain size and lattice constant along the alkyl-stacking direction. This could be due to the fact that the colloidal nanoparticles do not interfere with the bulk-heterojunction crystallization, or to the fact that the interference is not measurable at low (below 0.3 wt% for Au and below 0.1 wt% for Ag) nanoparticle concentrations.

References

1. Chen, C.-C. *et al.* An Efficient Triple-Junction Polymer Solar Cell Having a Power Conversion Efficiency Exceeding 11%. *Adv. Mater.* **26**, 5670–5677, (2014).
2. Carsten, D. & Vladimir, D. Polymer–fullerene bulk heterojunction solar cells. Rep. *Prog. Phys.* **73**, 096401, (2010).
3. Thompson, B. C. & Fréchet, J. M. J. Polymer-fullerene composite solar cells. Angew. *Chem.* **47**, 58–77, (2008).
4. Sariciftci, N. S., Smilowitz, L., Heeger, A. J. & Wudl, F. Photoinduced Electron Transfer from a Conducting Polymer to Buckminsterfullerene. *Sci* **258**, 1474–1476, (1992).
5. Keivanidis, P. E. *et al.* Dependence of Charge Separation Efficiency on Film Microstructure in Poly(3-hexylthiophene-2,5-diyl):[6,6]-Phenyl-C61 Butyric Acid Methyl Ester Blend Films. J. Phys. *Chem. Lett.* **1**, 734–738, (2010).
6. Gan, Q., Bartoli, F. J. & Kafafi, Z. H. Plasmonic-Enhanced Organic Photovoltaics: Breaking the 10% Efficiency Barrier. *Adv. Mater.* **25**, 2385–2396, (2013).
7. Wu, J. L. *et al.* Surface plasmonic effects of metallic nanoparticles on the performance of polymer bulk heterojunction solar cells. *ACS Nano* **5**, 959–967, (2011).
8. Wang, D. H. *et al.* Enhanced Power Conversion Efficiency in PCDTBT/PC70BM Bulk Heterojunction Photovoltaic Devices with Embedded Silver Nanoparticle Clusters. Adv. Energy. *Mater.* **1**, 766–770, (2011).
9. Wang, D. H. *et al.* Enhanced light harvesting in bulk heterojunction photovoltaic devices with shape-controlled Ag nanomaterials: Ag nanoparticles versus Ag nanoplates. *R. Soc. Chem. Adv.* **2**, 7268–7272, (2012).
10. Kim, C. H. *et al.* Silver nanowire embedded in P3HT:PCBM for high-efficiency hybrid photovoltaic device applications. *ACS Nano* **5**, 3319–3325, (2011).
11. Wang, D. H. *et al.* Enhancement of Donor–Acceptor Polymer Bulk Heterojunction Solar Cell Power Conversion Efficiencies by Addition of Au Nanoparticles. *Angew. Chem. Int. Ed.* **50**, 5519–5523, (2011).
12. Chou, C.-H. & Chen, F.-C. Plasmonic nanostructures for light trapping in organic photovoltaic devices. *Nanoscale* **6**, 8444–8458.
13. Jaegeler-Hoheisel, T., Selzer, F., Riede, M. & Leo, K. Direct Electrical Evidence of Plasmonic Near-Field Enhancement in Small Molecule Organic Solar Cells. *J. Phys. Chem. C* **118**, 15128–15135, (2014).
14. Jung, K. *et al.* Plasmonic Organic Solar Cells Employing Nanobump Assembly via Aerosol-Derived Nanoparticles. *ACS Nano* **8**, 2590–2601, (2014).
15. Chuang, M.-K., Lin, S.-W., Chen, F.-C., Chu, C.-W. & Hsu, C.-S. Gold nanoparticle-decorated graphene oxides for plasmonic-enhanced polymer photovoltaic devices. *Nanoscale* **6**, 1573–1579, (2014).
16. Liao, H.-C. *et al.* Nanoparticle-Tuned Self-Organization of a Bulk Heterojunction Hybrid Solar Cell with Enhanced Performance. *ACS Nano* **6**, 1657–1666, (2012).
17. Lilliu, S. *et al.* Dynamics of Crystallization and Disorder during Annealing of P3HT/PCBM Bulk Heterojunctions. *Macromolecule*s **44**, 2725–2734, (2011).
18. Agostinelli, T. *et al.* Real Time Investigation of crystallization and phase segregation dynamics in P3HT: PCBM solar cells during thermal annealing. *Adv. Funct. Mater.* **21**, 1701–1708, (2011).
19. Lilliu, S. *et al.* The Influence of Substrate and Top Electrode on the Crystallization Dynamics of P3HT:PCBM Blends. *Energy Procedia* **31**, 60–68, (2012).
20. Schuettfort, T. *et al.* Surface and Bulk Structural Characterization of a High-Mobility Electron-Transporting Polymer. *Macromolecules* **44**, 1530–1539, (2011).
21. Wang, T. *et al.* The development of nanoscale morphology in polymer:fullerene photovoltaic blends during solvent casting. *Soft Matter* **6**, 4128–4134, (2010).
22. Lilliu, S. *et al.* Effects of Thermal Annealing Upon the Nanomorphology of Poly(3-hexylselenophene)-PCBM Blends. *Macromol. Rapid Commun.* **32**, 1454–1460, (2011).
23. Wang, C. C. D. *et al.* Optical and electrical effects of gold nanoparticles in the active layer of polymer solar cells. *J. Mater. Chem.* **22**, 1206–1211, (2012).
24. Guilbert, A. A. Y. *et al.* Influence of Bridging Atom and Side Chains on the Structure and Crystallinity of Cyclopentadithiophene–Benzothiadiazole Polymers. *Chem. Mater.* **26**, 1226–1233, (2013).
25. Dane, T. G. *et al.* Oligo(aniline) nanofilms: from molecular architecture to microstructure. *Soft Matter*, **9**, 10501–10511, (2013).
26. SigmaAldrich, Gold Nanoparticles: Properties and Applications, (2014), (Date of access: 31/10/2014), <https://www.sigmaaldrich.com/>.
27. Kayunkid, N., Uttiya, S. & Brinkmann, M. Structural Model of Regioregular Poly(3-hexylthiophene) Obtained by Electron Diffraction Analysis. *Macromolecules* **43**, 4961–4967, (2010).
28. Kline, R. J. *et al.* Critical Role of Side-Chain Attachment Density on the Order and Device Performance of Polythiophenes. *Macromolecules* **40**, 7960–7965, (2007).
29. Sirringhaus, H. *et al.* Two-dimensional charge transport in self-organized, high-mobility conjugated polymers. *Nature* **401**, 685–688, (1999).
30. Zen, A. *et al.* Effect of Molecular Weight on the Structure and Crystallinity of Poly(3-hexylthiophene). *Macromolecules* **39**, 2162–2171, (2006).
31. Aryal, M., Trivedi, K. & Hu, W. Nano-Confinement Induced Chain Alignment in Ordered P3HT Nanostructures Defined by Nanoimprint Lithography. *ACS Nano* **3**, 3085–3090, (2009).

32. Chu, C.-W. *et al.* Control of the nanoscale crystallinity and phase separation in polymer solar cells. *Appl. Phys. Lett.* **92,** 103306–103303, (2008).
33. Rispens, M. T. *et al.* Influence of the solvent on the crystal structure of PCBM and the efficiency of MDMO-PPV:PCBM 'plastic' solar cells. *Chem. Commun.* **9,** 2116–2118, (2003).
34. Birkholz, M. *Thin Film Analysis by X-Ray Scattering.* (Wiley-VCH Verlag, 2005).

Acknowledgements

Author Contributions

M.S.D. financed S.L. and M.A. research activities through a Masdar Institute internal grant. S.L. and J.E.M. wrote the proposal for the beamtime and directed the experiments at the XMaS beamline. S.L. supervised and managed the project. S.L. and M.A. prepared the samples. S.L., M.A., M.S.D. and J.E.M. performed the measurements at the beamline. O.B. took care of the beamline setup and troubleshooting. S.L. and M.A. analyzed the XRD data and wrote the manuscript. S.L. upgraded his own software for GI-XRD analysis. All the authors helped with the manuscript editing.

Additional Information